SIMULATION AND ANALYSIS OF A LARGE AREA PLASMA SOURCE

by

V. P. Gopinath and M. A. Lieberman

Memorandum No. UCB/ERL M95/65

25 June 1995

SIMULATION AND ANALYSIS OF A LARGE AREA PLASMA SOURCE

by

V. P. Gopinath and M. A. Lieberman

Memorandum No. UCB/ERL M95/65

25 June 1995

ELECTRONICS RESEARCH LABORATORY

College of Engineering
University of California, Berkeley
94720

Simulation and Analysis of a Large Area Plasma Source

V. P. Gopinath and M. A. Lieberman
EECS Department, University of California,
Berkeley, CA 94720

June 25, 1995

1 Introduction to the Model

A large area plasma source (LAPS) is currently under development by the Plasma Assisted Materials Processing Group at U.C. Berkeley. A two dimensional representation of the source is shown in Figure 1. RF or microwave power, present in the eight cylindrical quartz tubes in the center, ionizes the surrounding gas to generate a plasma over a large area. The rectangular plasma chamber has dimensions $2d \times 8W$ where d can be varied and $W = 3$ inches (7.62 cm). The dashed square boxes surrounding the quartz tubes are a planar representation to facilitate the simulation. The silicon or glass substrate to be etched or deposited on is positioned at one or both of the longer sides. It is of some interest to be able to predict the uniformity of the flux of ions to the substrate surface as the distance d is varied. Typically, one can expect that for larger downstream distances, the uniformity of ions hitting the surface improves in the center of the substrate while the density drops at the edges. Therefore there is a trade-off between center and edge uniformity, which leads to an optimum choice of d for a given substrate of length $2l$. Further, the optimal distance d may vary depending upon the operating pressure regime. Therefore simulations can provide critical design information and some sort of figure of merit of the source.

2 Simulation

The ambipolar diffusion equation,

$$-D_a \nabla^2 n(x,y) = G(x,y), \tag{1}$$

is solved numerically over a rectangular grid, where $n(x,y)$ is the ion density, D_a is the ambipolar diffusion coefficient and $G(x,y)$ is the volume generation rate of ions in the system. This (Poisson's) equation may be solved numerically by assigning boundary conditions [1] to the edges and to the quartz tubes within the structure. For purposes of this simulation, all boundaries are considered particle absorbing. A more accurate representation of the quartz tubes and chamber walls, especially at lower pressures, would require a mixed boundary condition. In this case the calculated uniformity would increase.

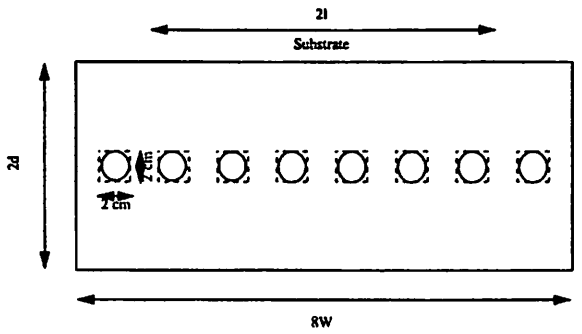

Figure 1: Large Area Plasma Source

The values of D_a and G depend upon the operating conditions of the source and can be broadly divided into three pressure regimes depending on the electron-neutral particle ionization length λ_{iz}. In an argon discharge, the pressure dependence of λ_{iz} is given approximately by

$$\lambda_{iz}(\text{cm}) = \frac{125}{p(\text{mTorr})}. \tag{2}$$

The ambipolar diffusion coefficient D_a is given approximately by

$$D_a(\text{cm}^2/\text{s}) = \frac{3.1 \times 10^6}{p(\text{mTorr})}, \tag{3}$$

and the generation rate G is given as

$$G(\text{cm}^{-3}\text{s}^{-1}) = \frac{2.6 \times 10^{18}}{A(\text{cm}^2)} \tag{4}$$

where the effective generation area A depends upon the pressure regime of operation. As will be seen below, the regime of operation switches from low to intermediate pressure range, depending upon the length d (in cm), at a pressure given by

$$p_{swtch}(\text{mTorr}) = \frac{125}{d-1}. \tag{5}$$

2.1 High Pressure Regime

When the operating pressure is greater than 44.5 mTorr, the ionization region is considered to be limited to eight small annular regions around the quartz tubes of thickness equal to the ionization length λ_{iz}. In this regime A is defined as

$$A(\text{cm}^2) = 8 \times [(2\lambda_{iz}+2)^2 - 2^2] = 32\lambda_{iz}(\lambda_{iz}+2) \tag{6}$$

2.2 Intermediate Pressure Regime

In the operating pressure range $p_{swtch} < p < 44.5$ mTorr, the ionization region is of height equal to $2+2\lambda_{iz}$ and length equal to $8W$, (with the cross sectional area of the eight quartz tubes excluded) and A is given by

$$A(\text{cm}^2) = 122\lambda_{iz} - 90 \tag{7}$$

2.3 Low Pressure Regime

In the low pressure operating pressure range $p \leq p_{swtch}$ mTorr, the ionization occurs everywhere inside the structure and A (excluding the cross sectional areas of the tubes) is given by

$$A(\text{cm}^2) = 16dW - 32. \tag{8}$$

3 Results

Simulations were run for the low, intermediate and high pressure regimes at 10 mTorr, 30 mTorr and 100 mTorr respectively. The fluxes of ions at $y = d$, with $d = 1.5W, 1.25W, W, 0.75W$ and $0.5W$, corresponding to 11.43, 9.525, 7.62, 5.715 and 3.81 cm respectively, were calculated. Uniformity was defined as

$$Uniformity = \Delta\Gamma_x/\bar{\Gamma}_x = 2 \times (Max - Min)/(Max + Min) \tag{9}$$

over the given length.

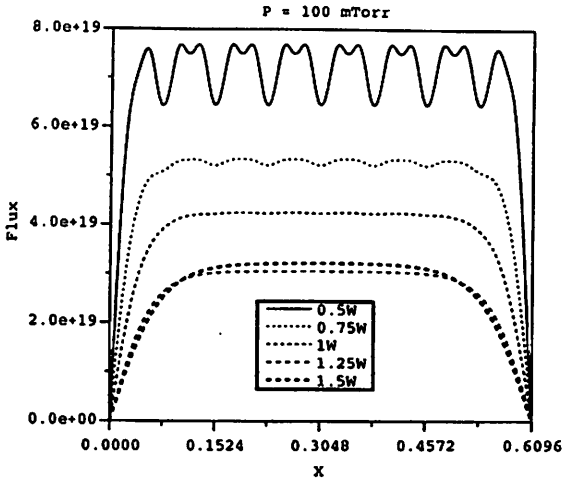

Figure 2: Results at $p = 100$mTorr

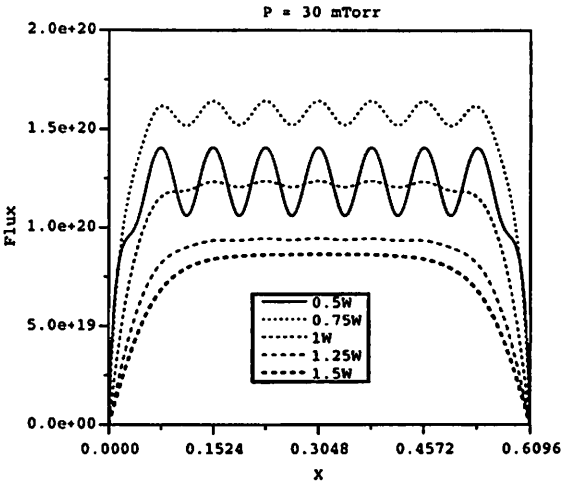

Figure 3: Results at $p = 30$mTorr

3.1 Results at 100 mTorr

The simulations run at 100 mTorr are shown in Figure 2. In this regime, the generation zone is limited to small annular regions surrounding the quartz tubes. It can been seen that while the central uniformity increases for locations further away from the generation area, the uniformity near the edge decreases. The location $d = 1.25W$ shows the most uniformity : less than 0.15% variation over 20 cm (centered around $X = 4W$). However, if a slightly higher degree of non-uniformity is acceptable, $d = W$ location provides 0.22% variation over a distance of 22 cm. Further, the location $d = 0.75W$, provides uniformity over the largest distance : 1.3% over 38 cm.

3.2 Results at 30 mTorr

The simulations run at 30 mTorr are shown in Figure 3. In this regime, the generation zone has a width equal to $2 + 2\lambda_{iz}$ and a length $8W$. Again, the location $d = 1.25W$ shows the most uniformity, 0.38% variation over 20 cm. The location $d = W$ exhibits a 1.25% variation over a distance of 30 cm. The location $d = 0.75W$, provides uniformity of 3.8% over 38 cm.

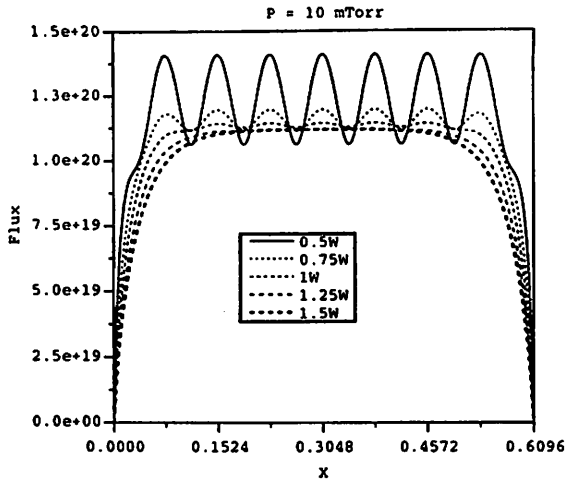

Figure 4: Results at p = 10mTorr

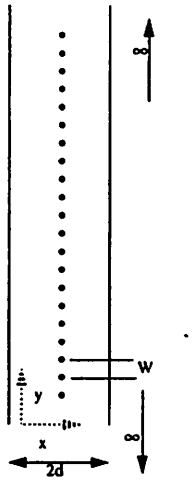

Figure 5: Infinite Number of Flux Sources

3.3 Results at 10 mTorr

The simulations run at 10 mTorr are shown in Figure 4. In this regime, the generation zone encompasses the whole structure. Hence the flux at the walls is seen to be the largest. As in the 100 mTorr and 30 mTorr case, $d = 1.25W$ provides the best uniformity; 0.15% variation over of 20 cm. The $d = W$ location shows 0.72% uniformity variation over of 30 cm. If 3.4% uniformity is acceptable, $d = 0.75W$ provides it over a very large distance; 46 cm, nearly 3/4 of the length of the system.

4 Analytic Models

Two analytic models can be used to compare with the simulation results. In both models the ionization source is localized to a set of equidistant δ-function sources separated by a spacing W. Hence these models are most applicable to the high pressure regime. For the simplest model, shown in Figure 5, we assume that there is an infinite set of singular (δ-function) flux sources located at $x = d$, $y = \pm mW$, m an integer. The density n satisfies Laplace's equation

$$\nabla^2 n = 0 \tag{10}$$

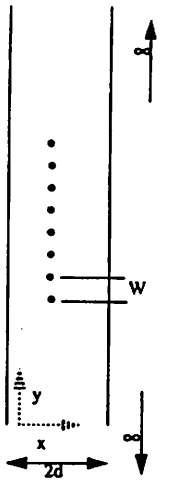

Figure 6: Finite Number of Line Sources with Infinite Walls

within $0 < x < d$, $-\infty < y < \infty$, and is assumed to vanish at $x = 0$. The appropriate solution of (10) is

$$n = A_0 \frac{x}{d} + \sum_{m=1}^{\infty} A_m \sinh \frac{2\pi m}{W} x \cos \frac{2\pi m}{W} y \,, \tag{11}$$

which has the flux

$$\Gamma_x = -D_a \frac{dn}{dx} = -\frac{A_0}{d} - \sum_{m=1}^{\infty} A_m \frac{2\pi m}{W} \cosh \frac{2\pi m}{W} x \cos \frac{2\pi m}{W} y \,. \tag{12}$$

We assume that at $x = d$, the x-flux is

$$\Gamma_x(d, y) = -\sum_{i=-\infty}^{\infty} \delta(y - iW) = -\frac{1}{W}\left(1 + 2\sum_{m=1}^{\infty} \cos \frac{2\pi m}{W} y\right) \,. \tag{13}$$

Equating (12) and (13) and solving for the coefficients A_m yields

$$A_0 = \frac{d}{W} \tag{14}$$

and

$$A_m = \frac{1}{\pi m \cosh \frac{2\pi m d}{W}} \,, \qquad m \neq 0 \,. \tag{15}$$

Provided $A_0 \gg A_1 \gg A_2$, then the flux incident on the surface $x = 0$ is found by inserting (14) and (15) into (12):

$$\Gamma_x(0, y) = -\frac{1}{W} - \frac{2}{W} \frac{1}{\cosh \frac{2\pi d}{W}} \cos \frac{2\pi}{W} y \,. \tag{16}$$

From (9) the predicted uniformity is then

$$\frac{\Delta \Gamma_x}{\bar{\Gamma}_x} = \frac{4}{\cosh \frac{2\pi d}{W}} \,. \tag{17}$$

The uniformity for a finite set of line sources (e.g., eight) can also be determined. Consider the model shown in Figure 6, consisting of a set of N (an even integer) equidistant line sources each separated by a spacing W, centered between two parallel planes at $x = \pm d$. The sources are located at $x = 0$, $y_m = \pm(m + \frac{1}{2})W$, m an integer $\leq N/2$. Consider first a single line source located at $x = 0$, $y = 0$. The potential and flux can be obtained from the complex function [2]

$$F = \ln \left[-\cot \frac{\pi z}{4d}\right] \,, \tag{18}$$

where $z = x + jy$ is the complex coordinate and

$$F = \psi + j\chi \,. \tag{19}$$

Here ψ is the potential, and the flux at the plane $x = d$ is given by

$$\Gamma_x = -\left(\frac{\partial \psi}{\partial x}\right)_{x=d} = -\left(\frac{\partial \chi}{\partial y}\right)_{x=d} \tag{20}$$

The latter form for Γ_x follows from the Cauchy-Riemann conditions. Superposing a set of eight sources, we have

$$F = \sum_{k=1,3,5,7} \left(\ln\left[-\cot\frac{\pi(z - jk/2)}{4d}\right] + \ln\left[-\cot\frac{\pi(z + jk/2)}{4d}\right]\right) \,, \tag{21}$$

Combining terms with the same value of k, we obtain

$$F = \sum_{k=1,3,5,7} \ln \frac{\cosh\frac{\pi k W}{4d} + \cos\frac{\pi z}{2d}}{\cosh\frac{\pi k W}{4d} - \cos\frac{\pi z}{2d}} \,. \tag{22}$$

Inverting the order of the sum and the logarithm, we obtain

$$F = \ln \prod_{k=1,3,5,7} \frac{\cosh\frac{\pi k W}{4d} + \cos\frac{\pi z}{2d}}{\cosh\frac{\pi k W}{4d} - \cos\frac{\pi z}{2d}} \,. \tag{23}$$

To determine the flux we evaluate (21) at $z = d + jy$ to obtain

$$F = \ln \prod_{k=1,3,5,7} \frac{\cosh\frac{\pi k W}{4d} - j\sinh\frac{\pi y}{2d}}{\cosh\frac{\pi k W}{4d} + j\sinh\frac{\pi y}{2d}} \tag{24}$$

Each of the four terms is of the form $\exp(j\phi_k)$, where

$$\phi_k = -2\tan^{-1}\frac{\sinh\frac{\pi y}{2d}}{\cosh\frac{\pi k W}{4d}} \tag{25}$$

Hence

$$\chi(d, y) = \mathrm{Im}\, F(d, y) = -2 \sum_{k=1,3,5,7} \tan^{-1}\frac{\sinh\frac{\pi y}{2d}}{\cosh\frac{\pi k W}{4d}} \tag{26}$$

Inserting (26) into (20), we obtain the flux at the wall,

$$\Gamma_x = \frac{\pi}{d} \sum_{k=1,3,5,7} \frac{\cosh\frac{\pi k W}{4d}\cosh\frac{\pi y}{2d}}{\cosh^2\frac{\pi k W}{4d} + \sinh^2\frac{\pi y}{2d}} \tag{27}$$

In Figure 7, this expression (solid line) is compared with the simulation result at $p = 100$ mTorr. There is good agreement between the numerical and analytical result. The preceding result for the flux is not accurate near the walls at $y = \pm 8W$, because the density $n = 0$ there in the actual system (see Fig. 1), contrary to the solution $n = \mathrm{Re}\, F$ given by (23). However, we can use the method of images to approximate the solution in this region by considering image planes located at $y = \pm 8W$. By superposition of their eight line sources with their sixteen negative images, eight located at $y > 8W$ and eight located at $y < 0$, we obtain

$$\begin{aligned}\Gamma_x = {} & \tfrac{\pi}{d}\textstyle\sum_{k=1,3,5,7} \frac{\cosh\frac{\pi k W}{4d}\cosh\frac{\pi y}{2d}}{\cosh^2\frac{\pi k W}{4d} + \sinh^2\frac{\pi y}{2d}} - \tfrac{\pi}{d}\textstyle\sum_{k=1,3,5,7} \frac{\cosh\frac{\pi k W}{4d}\cosh\frac{\pi (y-8W)}{2d}}{\cosh^2\frac{\pi k W}{4d} + \sinh^2\frac{\pi (y-8W)}{2d}} \\ & - \tfrac{\pi}{d}\textstyle\sum_{k=1,3,5,7} \frac{\cosh\frac{\pi k W}{4d}\cosh\frac{\pi (y+8W)}{2d}}{\cosh^2\frac{\pi k W}{4d} + \sinh^2\frac{\pi (y+8W)}{2d}} \,.\end{aligned} \tag{28}$$

In Figure 8, this expression (solid line) is compared with the simulation result at $p = 100$ mTorr. There is excellent agreement between the numerical and analytical result. The analysis over-estimates the flux due to its assumption of point sources. Further, the presence of finite sized sources leads to the simulation predicting higher flux at the edges as compared to the analysis. Actually, there are an infinite number of images along the y-axis. The result for the flux Γ_x in this case can be written in terms of elliptic functions, but the results are not very illuminating and will be omitted here.

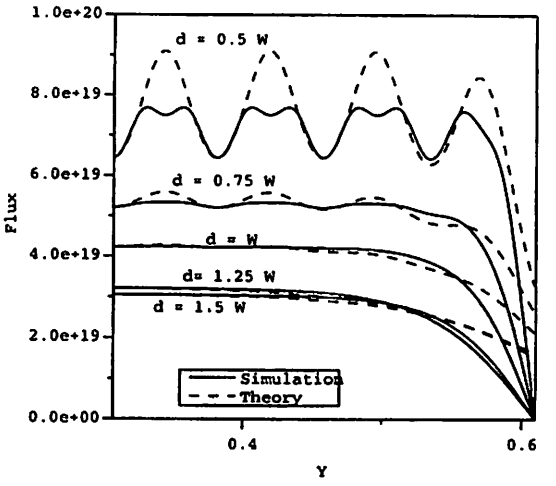

Figure 7: Comparison of Theory with Simulation at 100mTorr

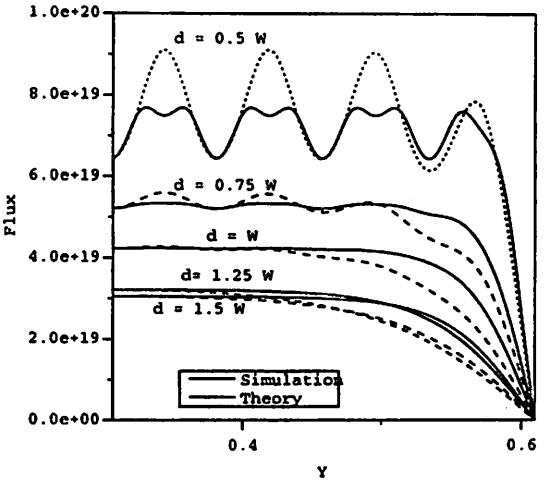

Figure 8: Comparison of Modified Theory with Simulation at 100mTorr

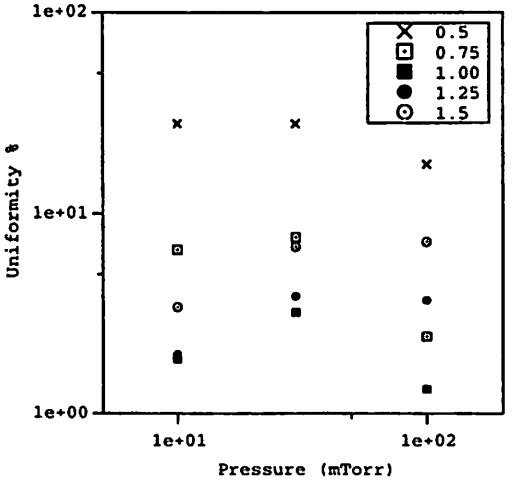

Figure 9: Flux Uniformity vs. Pressure at various d/W ratios for $2l = 36.5$ cm

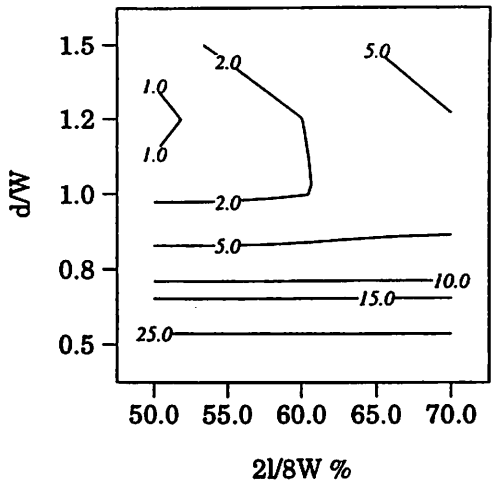

Figure 10: Contour map of Uniformity at $p = 10$mTorr

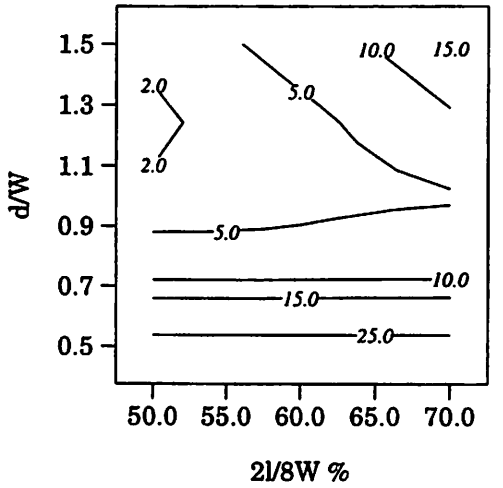

Figure 11: Contour map of Uniformity at $p = 30$mTorr

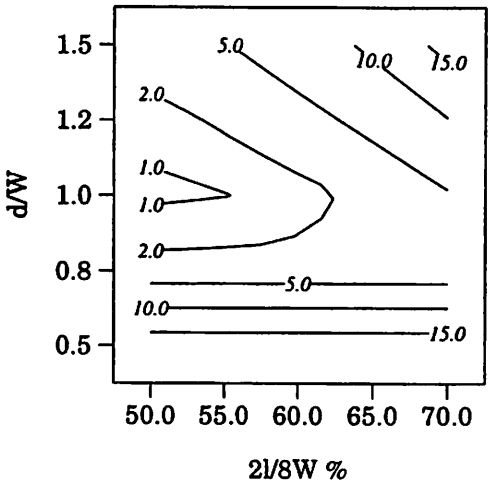

Figure 12: Contour map of Uniformity at $p = 100$mTorr

5 Conclusions

Figure 9 shows a plot of flux uniformity over a central distance of $2l = 36.5$cm (log scale) versus pressure (log scale) for $d/W = 0.5, 0.75, 1.0, 1.25$ and 1.5, which is useful in choosing d and W to optimize source performance. The results for $d = 0.5W$ show unacceptable uniformity at all three pressures. Location $d = W$ exhibits the best uniformity at all three pressures. It can be seen that $d = 0.75W$ shows better uniformity than $d = 1.25W$ at 100 mTorr. *Uniformity* vs. d values show an optimal value for $d = W$. The values of uniformity for the two extreme d points deteriorate for two different reasons. For a given $2l$ length, uniformity for larger d worsens due to edge effects. However, for smaller d, uniformity values deteriorate due to large fluctuations in flux. In order to understand the variation of uniformity with respect to $2l$, d/W and pressure, three contour maps are shown in Figures 10 – 12 corresponding to the uniformity at 10, 30 and 100 mTorr respectively.

6 Acknowledgment

This work was supported in part by ONR under Contract FD-N00014-90-J-1198, NSF grant ECS-92717500, DOE Grant DE-FG03-87ER13727, LLNL Grant W-7405-ENG-48, and a gift from Lam Research Corporation.

References

[1] W. H. Press, B. P. Flannery, S. A. Teukolsky and W. T. Vetterling, *Numerical Recipes in C, The Art of Scientific Computing*, p. 636-641 (Cambridge University Press, Cambridge, 1988)

[2] P.M. Morse and H. Feshbach, *Methods of Theoretical Physics*, Part II, p. 1235-8 (McGraw-Hill, New York, 1953).